IEEE Access
Multidisciplinary | Rapid Review | Open Access Journal

Received 28 January 2023, accepted 26 February 2023, date of publication 2 March 2023, date of current version 7 March 2023.

Digital Object Identifier 10.1109/ACCESS.2023.3251381

RESEARCH ARTICLE

Hole-Finding Learning Strategy for a Robot Assembly With Keyed Circular Peg

HAIBIN HUANG[1], HUAKANG CHENG[1], TONGTE WANG[1], TINGSHUO FU[1], AND CHAOSHENG ZOU[2]

[1]Institute of Mechanical and Automotive Engineering, Xiamen University of Technology, Xiamen 361024, China
[2]Xiamen Winjoin Technology Company Ltd., Xiamen 361025, China

Corresponding author: Huakang Cheng (2022031286@s.xmut.edu.cn)

This work was supported in part by the Natural Science Foundation of Fujian Province under Grant 2022J011244.

ABSTRACT Taking the gear assembly of the reducer assembly line as a research background, the hole-finding strategy for robot assembly with keyed circular pegs is proposed to solve the problem of low hole-finding efficiency and success rate. in the circular hole-finding task, deviation domains were divided based on a static mechanism, position vector trajectory optimization in the step distance and direction was designed, and a deviation domain-force mapping relationship was established using a genetic algorithm-support vector machine (GA-SVM) classification algorithm; the accuracy of this algorithm is approximately 90.00%. Thirty groups completed the circular hole-finding task in an average time of 5.4 s. For the square hole-finding task, dual monocular cameras were integrated to identify corner points of the flat key and keyway. Image semantic segmentation based on deep learning was used for the corner-point recognition of the flat key to suppress the effect of changes in light intensity; the recognition has an average error of 0.39 mm. Coarse and fine adjustment circumferential deflection strategies were adopted sequentially. The 30 groups of square hole-finding tasks exhibited a 96.70% success rate in an average time of 10.2 s. The proposed hole-finding strategy improves the efficiency and success rate of the gear assembly.

INDEX TERMS Keyed circular peg, learning-based robot hole finding, support vector machine, image semantic segmentation based on deep learning, genetic algorithm.

I. INTRODUCTION

Gears are widely used in mechanical components. The gear assembly is used in industrial robots as an alternative to manual labor. Overcoming robot end positioning errors and improving the efficiency and success rate of hole finding have become a challenge.

The existing research work on robot hole finding is divided into passive and active hole finding. The former is achieved by adding passive flexible actuators to the robot's end and by performing a "blind search" for the hole location using Archimedean spirals and grating-type trajectories [1], [2], [3]. However, this approach suffers from low efficiency; therefore, its use for hole finding remains limited. Active hole finding involves two steps: Constructing a peg-hole pose error model, which includes noncontact perspective projection [4], [5], [6], [7], contact mechanics [8], and data models. Zhu et al. [9] utilized a quad-core laser pointer and monocular vision to collect hole position information and to align rivets; they achieved a precision accuracy of 0.08 mm. Triyonoputro et al. [10] obtained the estimated hole lo-cation using multi-view images with a deep neural network model and achieved a circular peg-hole alignment with a clearance of 0.4 mm; however, this noncontact perspective projection model offers poor interference resistance and precision. Zhou et al. [11] established a mechanical mechanism model of the generator-frame double circular peg-hole contact issue and achieved a hole-finding success rate of 70.5%. Kim et al. [12] trained a position-force mapping model for a 3-mm square area using a clustering algorithm and achieved a model error of less than 0.35 mm. A peg-hole data model uses machine learning methods to train contact state data

The associate editor coordinating the review of this manuscript and approving it for publication was Turgay Celik.

offline and predict the current state online [13], [14], [15]. This model is updated in real time for online learning through data input from the current contact state [16], [17], [18], [19], [20]. Both online and offline data modeling are affected by large data quantities and the complexity of reverting model errors. Hole-finding trajectory optimization, which involves a feed step and direction optimization based on the hole-finding model [21]. Ding et al. [22] extracted optimal trajectory features using a Gaussian mixture model and dynamic motion primitive for trajectory generalization learning, and they achieved a hole-finding success rate of 83.3% for obstacle avoidance trajectories using a complicated trajectory optimization approach. The hole-finding objects listed above are mainly intended for peg hole structures with a single regular form and an oversized fit tolerance. The approach is not easily portable, and the efficiency and success rate should be improved.

Based on the existing literature, a keyed circular peg and gears in a reducer are considered the objects of hole finding in this study. This study aims to improve the success rate and efficiency of hole finding and accomplish circular and square hole finding in the centerline alignment of the circular peg and gear hole and in the circumferential registration of the key and keyway, respectively. To this end, a deviation domain-force/torque GA-SVM mapping discriminant data model is constructed using the static mechanism for dividing the deviation domain. Accordingly, a position vector trajectory optimization hole-finding approach is suggested. A dual monocular vision approach is adopted to detect the corner points of flat keys and keyways. The corner points help determine the circumferential deflection angle between the flat key and keyway. Further, an image semantic segmentation based on deep learning (ISSbDL) flat key corner point model with excellent accuracy and resistance to light intensity interference is designed. Finally, a circumferential coarse and refined deflection strategy is adopted in the given order to find the square hole. The strategy proposed in this paper improves the efficiency and success rate of combined hole finding for small clearance circular pegs with keys.

The remainder of this paper is organized as follows: In Section II, we describe the hole-finding problem and scheme. In Section III-A, we present circular hole-finding strategies involving algorithms for static mechanism analysis, force/torque-deviation domain mapping, and path planning. In Section III-B, we discuss the square hole-finding strategies involving algorithms for deflection angle identification and adjustment. Further, in Section IV, we discuss the experiments and the corresponding results. Finally, in Section V, we summarize the results of the current work and discuss the future research directions.

II. HOLE-FINDING SCHEME

A. HOLE-FINDING PROBLEM DESCRIPTION AND SCHEME DESIGN

As shown in Figure 1, the gearbox output mechanism consists of a keyed circular peg (60-mm circular peg and 0.1 mm

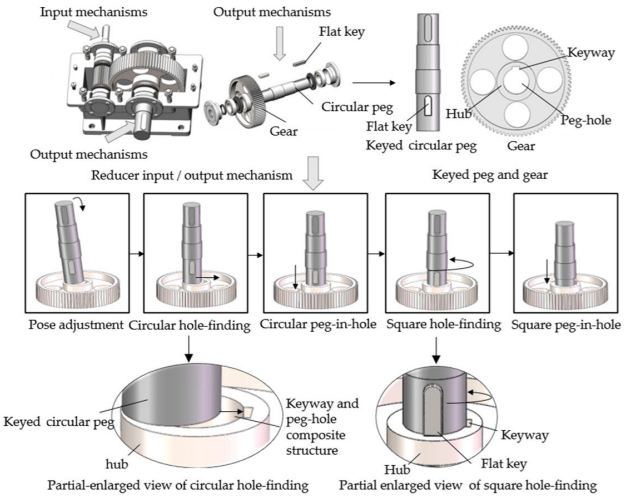

FIGURE 1. Assembly phase division and hole-finding problem.

fit tolerance) and a flat key (50 × 18 × 11 mm) with a circumferential fit tolerance of 0.05 mm. The assembly procedures for the keyed circular peg and gear include positional adjustment, circular hole finding (to align the peg and peg-hole centerlines), circular peg-in-hole, square hole finding (for the circumferential registration of key and keyway), and square peg-in-hole.

This study focuses on the circular and square hole-finding stages of assembly. In the circular finding-hole stage, the bottom face of the circular peg is in contact with the combined construction of the gear peg-hole and keyway; therefore, it is difficult to establish an accurate contact mechanics model. It is also challenging to formulate a trajectory optimization strategy. In the square hole-finding stage, the flat key has limited freedom of movement and can only rotate around the circumference. Further, the surface is prone to light-intensity interference, which makes it difficult to obtain the angle of deflection of the flat key and to perform the circumferential identification of the keyway, making it almost impossible to adjust the angle of deflection.

The design of the proposed scheme with the difficulties associated with hole finding is summarized below:

(1) Circular hole-finding stage: The position deviation of the circular peg and gear peg-hole is indicated by a position vector with the center of the lower end face of the circular peg (hereafter, center of the peg) as the start point and the center of the peg-hole (hereafter, center of the hole) as the endpoint. To find the circular hole, it is crucial to study changes in force/torque based on the position vector size and azimuth, create a mapping discriminant data model of the position deviation and force/torque, and produce a trajectory optimization strategy for the trajectory of the position vector in the step and direction.

(2) Square hole-finding stage: This stage involves identifying the deviation angle and adjusting the deviation. The deviation angle is the angle of the circle formed by the arc of the flat key and keyway corner points. In the proposed dual

monocular vision solution, the flat key and keyway corner points are identified for calculating the circumferential deviation angle. A circumferential coarse and refined deflection strategy is adopted in the given order to find the square hole.

B. HOLE-FINDING SYSTEM CONSTRUCTION

The robotic hole-finding system is shown in Figure 2. This system comprises robot clamping keyed circular pegs, a gear-fixing table, a double monocular vision module, a pneumatic element, and a computer, among other components. The robot clamping keyed circular pegs include a six-axis industrial robot with an end-mounted six-dimensional force sensor, an end camera to identify the corner points of the flat keys, and a pneumatic claw to realize real-time contact force detection. The gear support and fixing platform include a hole-finding platform, clamping gear cylinder, and a camera placed at the bottom. The bottom camera also recognizes keyway corners, and it detects misaligned gaps via the central through-hole in the support table, which forms the double monocular vision recognition module.

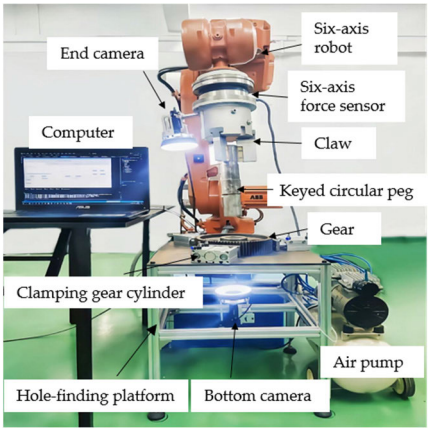

FIGURE 2. Robotic hole-finding system.

III. PROPOSED APPROACH

A. GA-SVM-BASED OPTIMIZATION OF POSITION VECTOR TRAJECTORIES FOR CIRCULAR HOLE-FINDING STRATEGIES

The static mechanism of force/torque variation based on the position vector size and the azimuth angle is analyzed in this section. The deviation domain is divided along the position vector size and azimuth angle, a GA-SVM mapping discriminant model of deviation domain-force and torque is established, and a strategy for optimizing the position vector trajectory to circular hole finding is proposed.

1) ANALYZING STATIC MECHANISM OF FORCE/TORQUE VARIATION WITH POSITION VECTOR

Figure 3 (a) shows the contact state of the circular peg and the gear, and Figure 3 (b) shows the bird's-eye view of the two-dimensional model of the peg-hole proposed by Simunovic and the corresponding assumptions: ignoring deformation and uniform distribution of forces along the contact surface [23]. These assumptions, together with the combined forces acting on the geometric center $D(D_x, D_y)$ of the contact surface, are used to analyze the forces in the contact state.

$$F_Z = F_1 \cos\sigma \approx F_1 \tag{1}$$
$$D_x = M_y / F_Z \tag{2}$$
$$D_y = M_x / F_Z \tag{3}$$

In equations (1)–(3), F_1 and α represent the combined force of the gears on the circular peg and the angle of inclination of the circular peg, respectively. Further, $\cos\sigma$ is almost equal to one because of the bottom camera's attitude adjustment. F_Z, M_x, and M_y represent the force and torque measured by the six-dimensional force sensor, and they correspond with the force and torque on the circular peg. ρ and θ represent the magnitude of the position vector beginning at the center of the peg O and terminating at O_1 and the azimuth, respectively. ρ varies when θ is constant, as indicated in Figures 3 (c) and (d). According to equations (2) and (3), when F_Z control is held constant, $|M_x|$ and $|M_y|$ decrease with a drop in |OD|. As shown in Figure 3 (d), $|M_x|$ and $|M_y|$ increase with an increase in |OD|. The trajectory $\theta = 0°$ begins (Figure 3 (e)) and continues until the conclusion of the trajectory at $\theta = 90°$ 3(f) when ρ is constant and θ is altered. Equations (2) and (3) show that $|M_x|$ grows with an increase in $|D_y|$ and $|M_y|$ decreases with a decrease in $|D_x|$. Here, $|D_x| = |D_y|$ (for this trajectory, $\theta = 45°$) and $|M_x| = |M_y|$. This analysis remains valid when θ changes from 0° to 360° over one week.

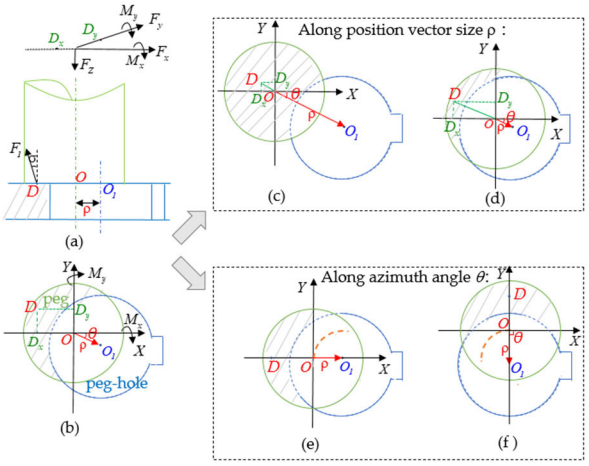

FIGURE 3. Mechanistic analysis of circular peg contact gears: (a) State diagram; (b) Bird's-eye view; (c) Increased ρ; (d) Decreased ρ; (e) Start point of trajectory ($\theta = 0°$); (f) End point of trajectory ($\theta = 90°$).

The six-dimensional force sensor used in this study is the ATI Omega 160, model SI-2500-400, with an accuracy error of Δ F = 0.0682N for force F and Δ M = 0.0076N-m for torque M. Then, the maximum position deviation of the peg center relative to the hole center at the end of the hole finding

can be theoretically calculated as

$$\Delta x_{\max} = \frac{\sqrt{M_x + M_y} + \Delta M}{F_z - \Delta F} \tag{4}$$

2) DEVIATION DOMAIN DIVISION AND POSITION VECTOR TRAJECTORY OPTIMIZATION

Figure 4 (a) shows that the center of the peg O is scattered around the center of the hole, which is searched blindly using multiple azimuths and position vector sizes because of the errors in the robot trajectory and orientation of the bottom camera. The contact moment and position deviation analysis are used to divide the deviation domain along ρ and θ (4(b) and 4(c)) and to develop an optimization strategy for the position vector trajectory (4(d) and 4(e)).

The deviation from location O compared to O_1 is distributed with O_1 as the center of the circle; here, the radius is less than 0.6 mm, θ does not change, $|M_x|$, $|M_y|$ decreases with an increase in ρ, and the fit tolerance of the circular peg and peg-hole is 0.1 mm, as indicated in Figure 4 (b). With O_1 as the center of the circle, the diameters of the large deviation domain, small deviation domain, and the coincidence domain are divided at diameters of 1.2 mm, 0.6 mm, and 0.1 mm, respectively. The value of ρ is constant, and θ ranges from 0° to 360° over a week. When $|D_x| = |D_y|$, $|M_x| = |M_y|$, $|M_x|$ increases with $|D_y|$, and $|M_y|$ decreases with $|D_x|$. Figure 4 (c) shows that the fit tolerance of the coincidence domain is divided into eight sectoral deviation domains and four linear deviation domains along θ.

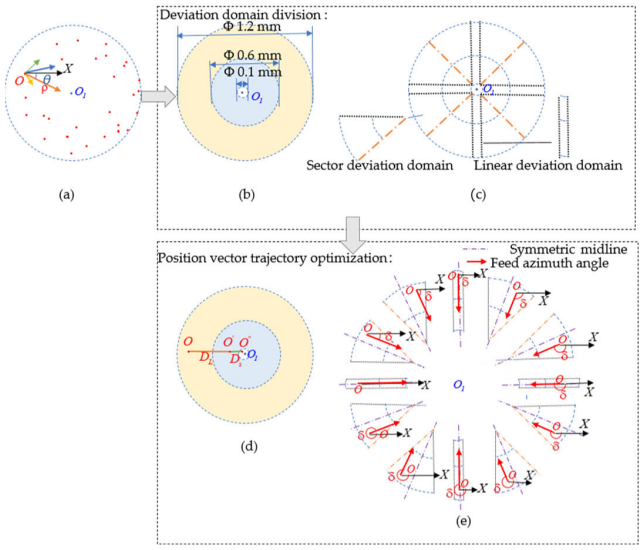

FIGURE 4. Deviation domain division and position vector trajectory optimization. (a) Peg center position deviation distribution and position vector; (b) Deviation domain division along ρ; (c) Deviation domain division along θ; (d) Set feed steps;(e) Set the feed azimuth angle.

Figure 4 (f) shows that the trajectory feed azimuth angles of the sector deviation and linear deviation domains are $\delta_i = 22.5° + 45°i, (i = 0, 1, 2, \ldots, 7)$ and $\delta_j = 0° + 90°j$, $(j = 0, 1, 2, 3, 4)$ respectively. We set a small deviation step $D_S = 0.08$ mm$D_S = 0.08$ *mm*, which is relatively less than the fit tolerance. The average number of steps to complete a circular hole finding task is set at a varying distance based on the trajectory feed azimuth and random deviation; the average number of steps is the lowest when the step of the large deviation is 0.4 mm. Thus, feed steps are set based on the large, small, and coincident deviation step of $D_L = 0.4$ *mm*, $D_S = 0.08$ *mm*, and $D_0 = 0$ *mm*, respectively, as illustrated in Figure 4 (e).

3) GA-SVM MAPPING DISCRIMINANT MODEL FOR DEVIATION DOMAIN-FORCE/TORQUE

A critical prerequisite for optimizing the trajectory of a circular hole finding task is to distinguish the deviation domain of the center of the peg based on the contact force/torque data. SVM offers a strong classification performance for tiny samples of force/torque data and linear multiclasses; the classifier aims to identify the best hyperplane in the feature space that maximizes the gap between samples.

The kernel function parameter (g) and penalty factor (C) have a considerable effect on the accuracy and generalization ability of SVM classification; the greater the value of C, the better is the data fitting, the larger is the value of g, and the lower is the classification accuracy. A genetic algorithm with heuristics is utilized in this study to discover the optimal C and g parameters for increasing the classification accuracy of SVM. The genetic algorithm employs several sets of starting population parameters to conduct a parallel search for enhancing the efficiency and circumventing the issue of slipping into the local optimum using selection, crossover, and variational global heuristics.

Figure 5 shows that the process of building the mapping discriminant model of the deviation domain-force/torque includes collecting force/torque data of each deviation do-main offline from the six-dimensional force sensor; selecting the force/torque affecting the circular hole finding; setting the corresponding deviation domain label as the training set; normalizing the measured data in the range [0,1] to remove the effect of data magnitude; inputting the normalized data into GA, grid search (GS), and particle swarm algorithm (PSO); identifying the optimal C and g parameters for the highest classification accuracy based on a detailed comparison; training SVM with the best parameters; and outputting the deviation domain-force/torque prediction set.

The simulation is performed using MATLAB, wherein 180 sets of data are gathered offline and normalized for each deviation domain independently. The first 150 sets of data as considered the training set, and the remaining 30, the test set. Figure 5(a) shows that the starting population size is set to 20, the maximum number of iterations is 100, and the parameters C and g are adjusted in the range [0,100] after binary coding, selection of high fitness (accuracy) populations, and cross-variation. Figure 5(b) indicates that the ideal GA parameters for a classification accuracy of 95.87% are C = 100.00 and g = 0.66. Compared to the best parameters C = 99.45 and g = 0.75 (d) for the PSO with the highest classification accuracy of 93.47% and the best parameters C = 97.62,

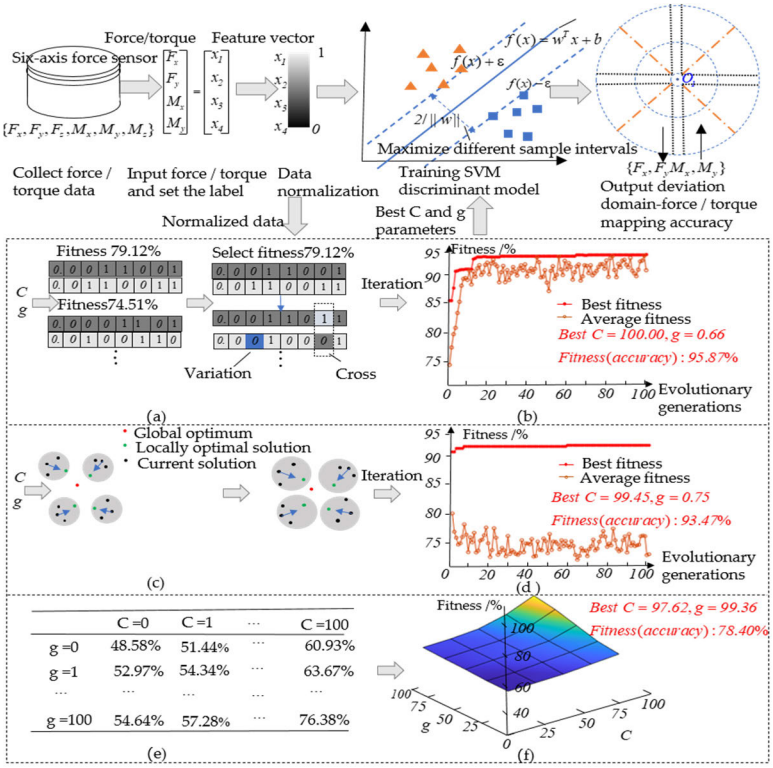

FIGURE 5. Mapping discriminant model for the deviation domain-force/torque. (a) GA search process for optimal parameters; (b) GA search for optimal parameter results; (c) PSO search process for optimal parameters; (d) PSO search for optimal parameter results; (e) GS search process for optimal parameters; (f) GS search for optimal parameter results.

g = 99.36 (f) for the GS with the highest classification accuracy of 78.40%. The best parameters C = 100.00 and g = 0.66 for GA were used to train the SVM model; these parameters produced a prediction set with a classification accuracy of 93.89%. The simulation results demonstrate the superiority of GA to find the reference compared to that using PSO and GS. The prediction accuracy of the SVM mapping discriminant model optimized using the GA parameters is 93.89%.

B. CIRCUMFERENTIAL SQUARE HOLE-FINDING STRATEGY BASED ON DUAL MONOCULAR VISION TO IDENTIFY CORNER POINTS

The anti-light intensity interference and high-precision ISSbDL flat-key corner point model based on encoding–decoding is developed in addition to the circumferential coarse-to-fine adjustable deflection angle square hole-finding strategy for dual monocular vision corner recognition.

1) FLAT KEY CORNER POINT MODEL FOR ISSBDL BASED ON ENCODING–DECODING

Traditional grey-level morphology-based image segmentation approaches are susceptible to light-intensity interference from flat key surfaces. These approaches cannot meet the accuracy requirements when extracting low-level features from images. Unlike conventional image segmentation algorithms, semantic segmentation classifies each pixel based on a specific object class, which helps solve the issue of light-intensity interference. Deep learning-based semantic segmentation helps extract high-level semantic features and enhance the precision of flat key corner-point segmentation.

As shown in Figure 6, an ISSbDL flat key corner point modelling procedure with an encoder-decoder architecture, image preprocessing (image annotation and parameter setup), model training, and model evaluation is employed in this study. The preprocessed images are sent to ISSbDL for training. The encoder in ISSbDL includes convolutional and pooling layers aimed at decreasing the size of the feature map and extracting the maximum amount of pixel-level semantic information as is feasible. The decoder includes convolutional, sampling, and classifier layers to recover the spatial dimension and fuse the encoded extracted characteristics for providing an input and output of the same size. The main metrics used to evaluate the model are loss and mean IoU. The mean IoU indicates the average ratio of the intersection and union of the predicted and labelled areas of the model. The loss indicates the difference between the predicted and actual values of the network model. The primary objective of training is to obtain minimum loss and maximum mean IoU.

Figure 6 shows the Halcon simulation platform developed for comparing the accuracy errors of ISSbDL and morphological approaches while segmenting flat critical

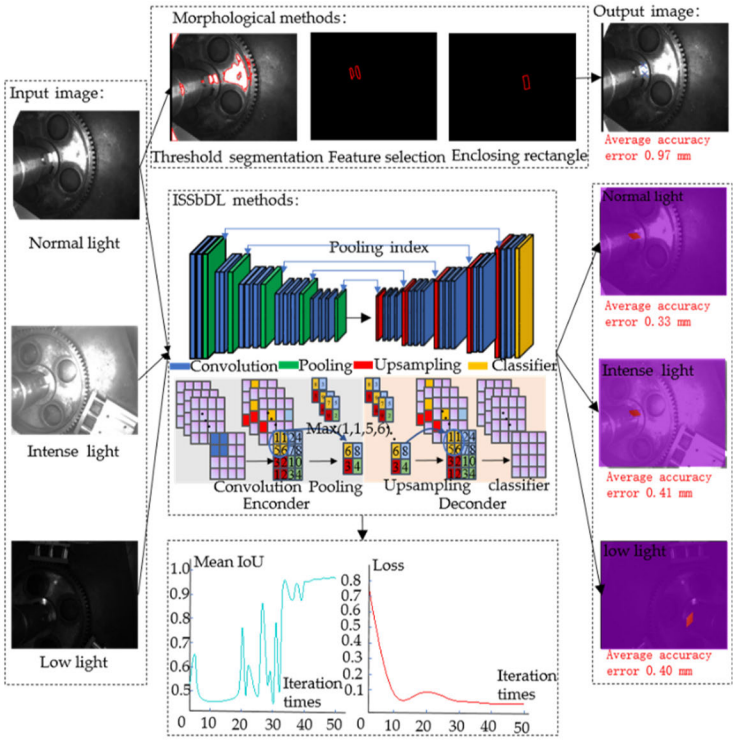

FIGURE 6. Corner point identification using ISSbDL and morphological methods at various light intensities.

corner points. A total of 200 flat key images with varying light intensities are labelled and entered into ISSbDL for training with the following parameters: training learning rate of 0.0001, batch size of 1, a training period of 50, the momentum of 0.99, weight of 0.00005, and image dimensions of [200, 150, 3]. The minimum loss is 0.038, and the maximum mean IoU is 0.947; this indicates a good training impact. The morphological method identifies corner points using binary threshold segmentation, shape feature region extraction, and minimum enclosing rectangle. Both methods recognize the same corner point in the 30 predicted images. Table 1 summarizes the comparison of the average accuracy error between the identified and actual corner point coordinates. The ISSbDL method identified corner point coordinates with an average accuracy error of 0.38 mm; the average accuracy errors under normal, low, and intense lights are 0.33 mm, 0.40 mm, and 0.41 mm, respectively; the average accuracy error of the morphological method is 0.97 mm; and the identification success rate is 76.74%. The simulation results suggest that ISSbDL enhances the resistance to light-intensity interference while recognizing corner points compared to that when using the morphological method.

2) CIRCUMFERENTIAL COARSE-FINE DEFLECTION ANGLE REGISTRATION STRATEGY BASED ON DUAL MONOCULAR VISION

Figures 7(a) and (b) illustrate the circumferential coarse-fine deflection angle registration flow chart 7(a) and schematic diagram 7(b) of the double monocular vision identified corner point. The end camera recognizes the corner point Q based on the ISSbDL flat key corner point model, and it coarsely changes the deflection angle α for the bottom camera to identify the keyway corner point P. Here, $\alpha = 2\arcsin PQ/2OP$ based on a geometric connection. Meanwhile, square hole finding is completed if the peg direction force reaches the set square hole-finding completion threshold. In contrast, the peg direction force does not reach the threshold because of corner recognition or circumferential trajectory errors. The bottom camera recognizes the corner point e_1e_2 in the bright area of the gap when the flat key is not registered as a square hole. Then, it fine tunes the deflection angle β to the peg direction force for reaching the set threshold with a fixed step distance of 0.04 mm; this is slightly less than the fit tolerance. At this moment, $\beta = 2\arcsin e_1e_2/2Oe_1$. If the gap is not recognized and the peg direction force does not reach the set threshold, they are fed in the predetermined direction (clockwise) and step distance until the peg direction force reaches the predetermined threshold, which helps discover the square hole.

IV. HOLE-FINDING EXPERIMENT

Experiments were conducted on the hole-finding platform shown in Figure 2 to demonstrate the effectiveness and rate of success for the proposed hole-finding strategy. We set the following thresholds to determine the completion of the hole: force F $\leq$ 0.10 N and torque M $\leq$ 0.01 N $\cdot$ m. We set

TABLE 1. Comparison of the precision error (E) of two methods for some identified corner points.

Real position	ISSbDL	Morphology	E-ISSbDL	E-Morphology	Light
(264.34, 227.68)	(264.17, 227.32)	(264.81, 226.77)	0.40	1.02	relatively strong
(268.25, 229.31)	(268.04, 228.95)	-	0.42	-	intense
(270.78, 230.69)	(270.52, 230.46)	(269.98, 230.26)	0.32	0.93	normal
(274.19, 233.05)	(273.97, 232.79)	(273.84, 232.22)	0.34	0.94	normal
(281.86, 241.51)	(281.57, 241.22)	-	0.41	-	low
(285.02, 247.82)	(285.30, 247.55)	(285.63, 247.07)	0.39	0.99	relatively low

* All units are in mm.

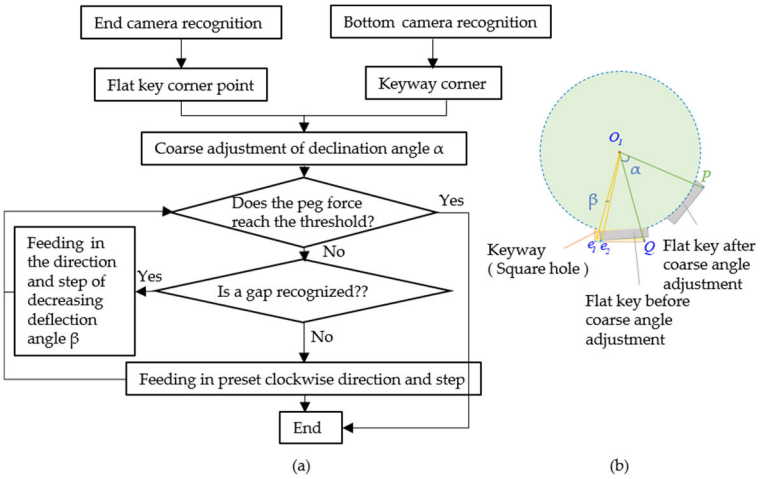

FIGURE 7. Circumferential coarse-fine deflection angle registration strategy based on dual monocular vision: (a) Flowchart for square hole finding based on dual monocular vision; (b) Square hole finding based on dual monocular vision.

thresholds so that the robot system stops when F $\geq$ 50N or M $\geq$ 5N $\cdot$ m.

A. CIRCULAR HOLE-FINDING EXPERIMENT

The circular hole-finding strategy compares the positionvector trajectory based on the GA-SVM, GS-SVM, PSOSVM mapping discriminant models, and the Archimedes' spiral trajectory, as indicated in Table 2. 30 sets of experiments were conducted; the average time of Archimedes' spiral trajectory (228.1 s) was greater than that of the position vector trajectory (8.2 s). These results indicate that the position vector trajectory optimization circular hole-finding strategy is highly effective. The average time of the position vector trajectory based on the GA-SVM mapping discrimination model is 5.4 s, which is less than the average times for the GS-SVM and PSO-SVM mapping discrimination models by 6.1 s and 2.4 s, respectively. Further, GA-SVM has a higher accuracy and success rate for the position vector trajectory hole-finding strategy.

Figures 8 (a) and (b) show the experimental diagrams of the position vector trajectory circular hole-finding process based on GA-SVM and the position vector trajectory based on GA-SVM, GS-SVM, and PSO-SVM mapping discriminant models, respectively. The starting deviation A (252.81 mm, 260.23 mm) is followed by $\delta_i = 67.5°$ $(i = 1)$, $D_L = 0.4$ mm trajectory to B (252.96 mm, 259.86 mm); $\delta_i = 22.5°$ $(i = 0)$, $D_S = 0.08$ mm trajectory to C (253.04 mm, 259.83 mm); $\delta_j = 0°$ $(j = 0)$, $D_S = 0.08$ mm trajectory to D (253.12 mm, 259.83 mm) and E (253.20 mm, 259.83 mm). The GA-SVM mapping discriminant model based on the position vector trajectory circular hole-finding requires 6.4 s for hole-finding. Figure 8 (c) shows the force/ torque variation over time for the group's GA-SVM mapping discriminant model based on the optimized position vector trajectory in circular hole-finding process. F_x and F_y are mainly related to the contact friction. In A_1B_1 to C_1D_1 process, as equivalent ρ decreases, θ decreases to 0°, then M_x decreases to fluctuates around the threshold, while M_y remains constant at a high value. In the D_1E_1 process, M_y drops sharply at 5.9 s before stabilizing at 6.4 s to reach the threshold value for the circular hole-finding process. The variations of force or torque with time during the circular hole-finding process is in accordance with the mechanistic analysis. The Archimedes spiral trajectory as 261 s, whereas the GS-SVM and PSO-SVM mapping discriminant models take 11.8 s and 7.9 s to optimize the position vector trajectory, respectively.

TABLE 2. Comparison of experimental results of different methods for circular hole finding.

Methods		Accuracy /%	Successful hole-finding	Average time/s
Position vector trajectory	(GA-SVM)	90.00	Yes	5.4
	(GS-SVM)	73.34	Yes	11.5
	(PSO-SVM)	86.67	Yes	7.8
Archimedes spiral trajectory		-	Yes	228.1

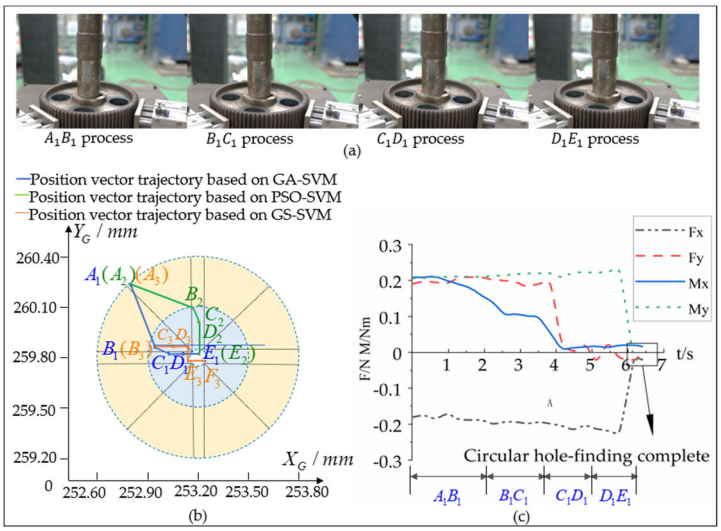

FIGURE 8. Group of hole-finding experiments: (a) GA-SVM-based position vector trajectory circular hole-finding process; (b) Position vector trajectories-based three mapping discriminant models; (c) GA-SVM-based plot of force/torque variation with time during a position vector trajectory.

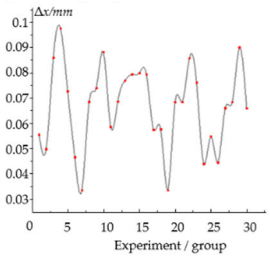

FIGURE 9. Error in the actual position of the peg center relative to the hole center Δx for 30 sets of experiments.

As shown in Figure 9, the maximum position deviation Δx of the peg relative to the hole center after the 30 sets of experimental hole findings is counted. Considering sensor uncertainties, the Δx values are within a clearance range of 0.1 mm for force-guided peg-in-hole tasks.

B. SQUARE HOLE-FINDING EXPERIMENT

Table 3 summarizes the comparison results of the circumferential square hole-finding strategies for dual monocular visual recognition and blind search. Both ISSbDL and morphological approaches are used for a flat key angle point detection in dual monocular visual recognition. In 30 sets of experiments conducted under varying light intensities, the average time of the blind search (435.2 s) is longer than the average time of square hole finding using dual monocular visual recognition (14.0 s). The success rate is 96.70%, the model is 7.6 s faster, and the precision is 20% higher than that of the dual monocular hole-finding strategy based on morphology. The ISSbDL-based dual monocular square hole-finding strategy achieves good efficiency and a high success rate.

Figure 10 (a) shows the experimental diagram of the ISSbDL-based dual monocular square hole-finding, and Figure 10 (b) depicts the square hole-finding trajectory of the process. The bottom camera identifies the corner point Q (262.36 mm, 225.23 mm), and the end camera identifies the corner point P_1 (288.55 mm, 257.03 mm) based on the ISSbDL flat key corner; the precision error is 0.37 mm. The coarse-adjustment deflection angle $\alpha = 71.96°$ and the detection peg direction force does not reach the threshold. The bottom camera detects the clearance corner points e_1 (244.19 mm, 225.40 mm) and e_2 (244.83 mm, 225.40 mm) with a 0.04 mm step distance based on the direction of $\beta = 0.52°$ reductions until the peg direct force reaches the threshold. The dual monocular square hole-finding based on ISSbDL requires 10.8 s. According to the 17.1 s required for the morphological double monocular square hole finding, a blind search requires 417.6 s. Figure 10 (c) shows that the entire F_x, F_yM_x, M_y process fluctuates within the threshold when detecting the change in F_x, F_y, F_Z, M_x, M_y with time for this process. The P_1Q coarse-adjustment deflection angle

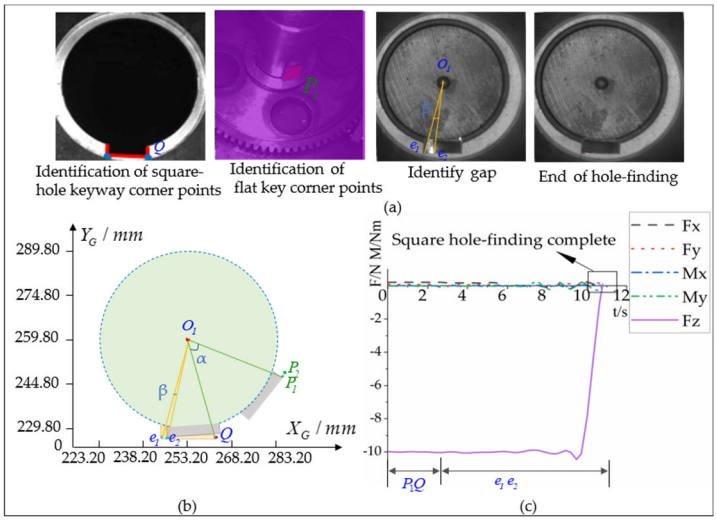

FIGURE 10. Group of square hole-finding experiments: (a) ISSbDL-based dual monocular vision recognition for square hole finding; (b) ISSbDL-based on dual monocular vision recognition for square hole-finding trajectories; (c) ISSbDL-based dual monocular visual recognition of square hole finding force/torque over time.

TABLE 3. Comparison of the experimental results of the different methods of finding square holes.

Methods		Success rate /%	Average precision error /mm	Average time/s
dual monocular vision	(ISSbDL)	96.70	0.39	10.2
	(morphology)	76.70	0.99	17.8
blind search		-	-	435.2

process requires 2.2 s, and the e_1e_2 fine adjustment process requires 8.4 s; at 10.6 s, F_z drops sharply from 10 N, and at 10.8 s, it reaches the square hole-finding threshold with stability.

V. CONCLUSION

A 60-mm circular peg (tolerance = 0.1 mm) and a 52 × 18 × 11 mm flat key (circumferential tolerance = 0.05 mm) was used to compose the keyed circular peg. The circular peg and gear peg-hole are aligned along the centerline, and the key and keyway are registered along the circumference.

1) The GA-SVM mapping discriminant model of the deviation domain-force/torque is developed based on the static mechanism for dividing the deviation domain; an optimum circular hole-finding strategy for position vector trajectory in the step and direction was also provided. The simulation of 30 sets of experiments confirmed that a circular hole finding was successfully achieved with 90% GA-SVM precision. The average efficiency of the circular hole was 5.4 s, 41.2-times shorter than the average efficiency of the Archimedes spiral trajectory and 6.1 s and 2.4 s shorter than the average efficiency of the position vector trajectory optimization strategy based on the GS-SVM and PSO-SVM models, respectively.
2) We established an ISSbDL flat key corner model, dual monocular visual identification corner, and the circumferential coarse to fine adjusting square hole-finding approach. After 30 sets of experiments, the average accuracy error of the ISSbDL method was 0.39 mm (0.60 mm shorter than the average accuracy of the morphological method).The average efficiency and success rate of the ISSbDL-based dual monocular square hole-finding strategy were 10.2 and 96.70%, respectively. Compared to the circumferential blind search, the efficiency and average efficiency of the dual monocular square hole-finding strategy based on morphology were reduced by a factor of 41.7 and 7.6 s; the success rate was enhanced by 20.00%.

The proposed circular and square hole-finding strategies achieved high success rates and excellent efficiency, and it helped identify some reference values for robot hole-finding using a keyed circular peg. This study has the limitation that hole finding requires a visual attitude adjustment prior to separating the hole finding assignment into two phases, circular hole finding and square hole finding, which complicates the hole finding processes. In the future, an intelligent hole-finding approach will be suggested to combine circular hole finding and square hole finding into a single operation to increase efficiency and success rates.

REFERENCES

[1] K. Van Wyk, M. Culleton, J. Falco, and K. Kelly, "Comparative peg-in-hole testing of a force-based manipulation controlled robotic hand," *IEEE Trans. Robot.*, vol. 34, no. 2, pp. 542–549, Apr. 2018.

[2] B. Baksys, J. Baskutiene, and S. Baskutis, "The vibratory alignment of the parts in robotic assembly," *Ind. Robot*, vol. 44, no. 6, pp. 720–729, 2017.

[3] S. Wang, G. Chen, H. Xu, and Z. Wang, "A robotic Peg-in-Hole assembly strategy based on variable compliance center," *IEEE Access*, vol. 7, pp. 167534–167546, 2019.

[4] K. Wang, D. Liu, Z. Liu, G. Duan, L. Hu, and J. Tan, "A fast object registration method for augmented reality assembly with simultaneous determination of multiple 2D–3D correspondences," *Robot. Comput.-Integr. Manuf.*, vol. 63, Jun. 2020, Art. no. 101890.

[5] P. Cirillo, G. Laudante, and S. Pirozzi, "Vision-based robotic solution for wire insertion with an assigned label orientation," *IEEE Access*, vol. 9, pp. 102278–102289, 2021.

[6] Y. Fan, X. Lv, J. Lin, J. Ma, G. Zhang, and L. Zhang, "Autonomous operation method of multi-DOF robotic arm based on binocular vision," *Appl. Sci.*, vol. 9, no. 24, p. 5294, Dec. 2019.

[7] W. Sun, Z. Zhang, and W. Zhang, "A coaxial alignment method for large flange parts assembly using multiple local images," *IEEE Access*, vol. 9, pp. 16716–16727, 2021.

[8] Q. Wang, R. Hou, J. Li, Y. Ke, P. G. Maropoulos, and X. Zhang, "Positioning variation modeling for aircraft panels assembly based on elastic deformation theory," *Proc. Inst. Mech. Eng., B, J. Eng. Manuf.*, vol. 232, no. 14, pp. 2592–2604, Dec. 2018.

[9] W. Zhu, H. Liu, and Y. Ke, "Sensor-based control using an image point and distance features for rivet-in-hole insertion," *IEEE Trans. Ind. Electron.*, vol. 67, no. 6, pp. 4692–4699, Jun. 2020.

[10] J. C. Triyonoputro, W. Wan, and K. Harada, "Quickly inserting pegs into uncertain holes using multi-view images and deep network trained on synthetic data," in *Proc. IEEE/RSJ Int. Conf. Intell. Robots Syst. (IROS)*, Nov. 2019, pp. 5792–5799.

[11] B. Zhou, L. Liu, and G. Chen, "Contact analysis for dual peg-in-hole assembly of automobile alternator frame," *Mech. Ind.*, vol. 21, no. 2, pp. 1–16, 2020.

[12] K. Kim, J. Kim, T. Seo, H. S. Kim, and J. Kim, "Development of efficient strategy for square peg-in-hole assembly task," *Int. J. Precis. Eng. Manuf.*, vol. 19, no. 9, pp. 1323–1330, Sep. 2018.

[13] M. Q. Mohammed, L. C. Kwek, S. C. Chua, A. Al-Dhaqm, S. Nahavandi, T. A. E. Eisa, M. F. Miskon, M. N. Al-Mhiqani, A. Ali, M. Abaker, and E. A. Alandoli, "Review of learning-based robotic manipulation in cluttered environments," *Sensors*, vol. 22, no. 20, p. 7938, Oct. 2022.

[14] W. Wu, H. Zhou, Y. Guo, Y. Wu, and J. Guo, "Peg-in-hole assembly in live-line maintenance based on generative mapping and searching network," *Robot. Auto. Syst.*, vol. 143, Sep. 2021, Art. no. 103797.

[15] Z. Zhang, G. Peng, W. Wang, Y. Chen, Y. Jia, and S. Liu, "Prediction-based human–robot collaboration in assembly tasks using a learning from demonstration model," *Sensors*, vol. 22, no. 11, p. 4279, Jun. 2022.

[16] Z. Wang, F. Li, Y. Men, T. Fu, X. Yang, and R. Song, "Deep deterministic policy gradient with reward function based on fuzzy logic for robotic peg-in-hole assembly tasks," *Appl. Sci.*, vol. 12, no. 6, p. 3181, Mar. 2022.

[17] Y. Wang, C. C. Beltran-Hernandez, W. Wan, and K. Harada, "Hybrid trajectory and force learning of complex assembly tasks: A combined learning framework," *IEEE Access*, vol. 9, pp. 60175–60186, 2021.

[18] F. Aschersleben, R. Griemert, F. Gabriel, and K. Dröder, "Reinforcement learning for robotic assembly of fuel cell turbocharger parts with tight tolerances," *Prod. Eng.*, vol. 14, no. 4, pp. 407–416, Oct. 2020.

[19] J. Xu, Z. Hou, W. Wang, B. Xu, K. Zhang, and K. Chen, "Feedback deep deterministic policy gradient with fuzzy reward for robotic multiple peg-in-hole assembly tasks," *IEEE Trans. Ind. Informat.*, vol. 15, no. 3, pp. 1658–1667, Jul. 2019.

[20] F. Li, Q. Jiang, S. Zhang, M. Wei, and R. Song, "Robot skill acquisition in assembly process using deep reinforcement learning," *Neurocomputing*, vol. 345, pp. 92–102, Jun. 2019.

[21] P. Guo, Z. Zhang, Y. Liu, Y. Liu, D. Zhu, and C. Shao, "A skill programming method based on assembly motion primitive for modular assembly system," *IEEE Access*, vol. 9, pp. 101369–101380, 2021.

[22] G. Ding, Y. Liu, X. Zang, X. Zhang, G. Liu, and J. Zhao, "A task-learning strategy for robotic assembly tasks from human demonstrations," *Sensors*, vol. 20, no. 19, p. 5505, Sep. 2020.

[23] S. Sergio, "Part mating theory for robot assembly," in *Proc. 9th ISIR*, 1979, pp. 183–193.

HAIBIN HUANG received the Ph.D. degree in measuring and testing technologies from Xiamen University, in 2011.

He is currently an Associate Professor with the School of Mechanical and Automotive Engineering, Xiamen University of Technology. His research interests include robot control technology, intelligent control algorithm research, and engineering application.

HUAKANG CHENG received the B.S. degree in automotive engineering from the Hefei University of Economics, in 2020. He is currently pursuing the M.S. degree with the School of Mechanical and Automotive Engineering, Xiamen University of Technology.

His research interests include intelligent assembly technology and image processing algorithms for robots.

TONGTE WANG received the B.S. degree in mechanical design-manufacture and automation from the Shaoxing University of Arts and Science, in 2018. He is currently pursuing the M.S. degree with the School of Mechanical and Automotive Engineering, Xiamen University of Technology.

His research interests include robot end-effector design and parallel robot research.

TINGSHUO FU received the B.S. degree in automotive engineering from the Huaiyin University of Technology, in 2020. He is currently pursuing the M.S. degree with the School of Mechanical and Automotive Engineering, Xiamen University of Technology.

His research interests include robot control technology and assembly platform design.

CHAOSHENG ZOU received the M.S. degree in electrical engineering specialty from the Qinyi University of Science and Technology, in 2015.

He is currently an Executive Director, the Chairperson, and the General Manager of Xiamen Winjoin Technology Company Ltd. His research interests include research on assembly technology and engineering application of industrial robots.